Reflection based lab-in-fiber sensor integrated in surgical needle for biomedical applications

PABLO ROLDÁN-VARONA[1,3,*], LUIS RODRÍGUEZ-COBO[2], AND JOSÉ MIGUEL LÓPEZ-HIGUERA[1,2,3]

[1] Photonics Engineering Group, University of Cantabria, 39005, Santander, Spain
[2] CIBER-bbn, Instituto de Salud Carlos III, 28029, Madrid, Spain
[3] Instituto de Investigación Sanitaria Valdecilla (IDIVAL), 39011, Santander, Spain
[*] Corresponding author: pablo.roldan@unican.es

Compiled July 2, 2020

Recently, lab-in-fiber (LIF) sensors have offered a new paradigm in many different scenarios, such as optofluidics, thanks to its ability to integrate different multi-physics sensor elements in a small space. In this Letter, the design and manufacture of a multiparameter sensing device is proposed, through the combination of an in-fiber air microcavity and a plane-by-plane (Pl-b-Pl) fiber Bragg grating (FBG). The reflection-based sensor, with a length less than 300 μm, is located at the end of a single-mode fiber (SMF), and integrated into a surgical needle for exploitation in biomedical applications. Here we present, to our knowledge, the first ultra-short LIF sensor reported under the "*touch and measure*" approach. In this first prototype, the detection of axial tensile strain (6.69 pm/$\mu\varepsilon$ in air cavity) and surrounding refractive index (11.5 nm/RIU in FBG) can be achieved simultaneously.

http://dx.doi.org/10.1364/ao.XX.XXXXXX

In recent times there has been a remarkable growth in the development of lab-on-chip (LOC) platforms, which have a high impact in multiple fields, such as biology, chemistry, or clinical procedures, among others [1, 2]. These types of platforms are characterized by the wide functionality given by the ability to integrate numerous sensor elements in a small space. As a result, lab-in-fiber (LIF) systems arise, which integrate the advantages of optical fibers in the manufacture of elements that enable multifunctional sensing [3]. The presence of the fiber core as a waveguide allows the different optofluidic sensor components to be interconnected optimally [4].

A widely used approach to the creation of three-dimensional structures in optical fibers is the femtosecond (fs) laser. It offers great simplicity and flexibility when inscribing patterns directly inside the bulk volume of transparent materials [5]. The induced refractive index changes (RIC) can create gratings or waveguides, which can lead to optofluidic microchannels (selective chemical etching), all with great potential in biomedical applications. An important fact in sensors used for these applications is that they should exhibit a reflection detection mode. In this way, those sensors could be used in a minimally invasive process.

There are several works in the literature that allow multiparameter sensing as a consequence of the integration of in-fiber air cavities and FBGs. Two sensors stand out, both manufactured by Liao *et al.* in 2010 [6], and 2013 [7]. The first sensor corresponds to an FBG that has an integrated Mach-Zehnder interferometer formed by a half-core trough-hole (transmission detection mode) [6]. The second one is a tunable phase-shifted FBG based on a in-grating through-hole bubble (reflection detection mode) [7]. However, the length of these sensors is 4 mm and 5 mm, respectively, more than 13 times greater than the manufactured sensor, and the strain sensitivity is lower (0.48 pm/$\mu\varepsilon$).

In this Letter, the design and manufacture of an ultra-short reflection-based LIF sensor integrated in a surgical needle for multiparameter sensing is detailed. The device, located in a single mode fiber (SMF), contains an in-fiber air bubble that acts as a Fabry-Perot microcavity, as well as a plane-by-plane (Pl-b-Pl) fiber Bragg grating (FBG) in the tapered fiber end (Fig. 1). Thus, in a clinical procedure, it is possible to determine the *touch* of the fiber with a tissue, and the *measurement* of the surrounding refractive index (SRI) ("*touch and measure*" approach). To the best of our knowledge, it is the first ultra-short reflected-based LIF sensor (< 500 μm) that enables simultaneous sensing of axial tensile strain and SRI. A numerical study of the light propagation in the sensor elements is carried out in order to optimize the final structure and validate the experimental results.

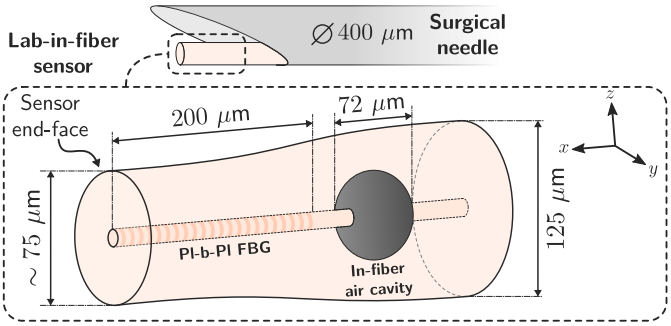

Fig. 1. Schematic view of the manufactured LIF sensor. It contains an in-fiber air bubble (Fabry-Perot cavity) and a Pl-b-Pl FBG in the tapered final section of the fiber. The sensor is integrated into a ⌀400 μm surgical needle.

The air bubble can be understood as an in-fiber Fabry-Perot interferometer (FPI). There are many more configurations apart from the air cavity used in the present work, such as hollow tubes, hollow-core photonic crystal fibers or tapered optical fibers. All of them stand out for their high sensitivity in a structure of small dimensions, as well as for a linear response and a possible reflection mode of detection [8].

In the manufactured LIF, the air microcavity allows the axial strain to be detected in the fiber end ("*touch*"). This parameter is protected from cross-sensivity error with radial strain, since the fiber is embedded in the needle. The incident light that is transmitted by the fiber core is reflected in each of the two fiber-air interfaces ($|\mathrm{RIC}| \simeq 0.45$). Both optical paths recombine in reflection, resulting in an interference pattern whose free spectral range (FSR) is defined by the well-known equation:

$$\mathrm{FSR} \simeq \frac{\lambda^2}{n \cdot 2L}, \quad \text{with} \quad \begin{cases} n = 1 \ (\text{cavity refractive index}) \\ L = \varnothing \ \text{cavity} \ (\text{diameter}) \end{cases}, \qquad \textbf{(1)}$$

where $2L$ is the difference of optical paths.

The second structure corresponds to the FBG located in the tapered fiber section (between air bubble and fiber end-face). The fiber tapering process makes it possible to increase the SRI sensitivity ("*measure*"). Its length is small enough that the Bragg wavelength (λ_B) reflection is greater than the interference pattern of the in-fiber air cavity ($\simeq 1\%$ of the incident light power).

The elements of the LIF sensor are depicted in Fig. 1. However, the physical dimensions and the relative situation of each sensor element has been optimized from the electromagnetic point of view in order to maximize reflection, limiting losses as much as possible. To this end, simulations using Finite Element Beam Propagation Method (FE-BPM) have been carried out in the COMSOL Multiphysics software. The maximum element size in the mesh is 0.19 μm ($\leq \lambda/8$).

The most restrictive element in terms of losses is the in-fiber air bubble. Consequently, a study of the electric field is performed by varying the cavity diameter and the wavelength (operating in C-Band). Specifically, it is performed a study for circular air-cavities of 50, 70 and 90 μm in diameter, as well as a square bubble (unreal) with 90 μm side. The electromagnetic study, shown in Fig. 2, has been carried out in the wavelength range between 1520 and 1570 nm. According to the results, it is observed that the best behavior in terms of reflection and losses is that corresponding to the square bubble (proof-of-concept of an ideal performance) (Fig. 2(d)). This is because the RIC interface of the two reflective surfaces is perfectly perpendicular to the longitudinal axis of the fiber. In this way, reflections towards the cladding, which lead to losses, are minimized. These unwanted reflections towards cladding increase as the cavity diameter decreases, as observed in the simulations corresponding to circular cavities. The power confinement in the central part of the bubble (and therefore in the posterior section of the fiber core) improves as the bubble diameter increases, up to the ideal case. Likewise, cavity lengths of 45.26, 70.69 and 90.35 μm have been determined by post-processing the FSR of the reflection patterns of the circular air cavities (Fig. 2(e)). It corresponds to relative errors (ϵ_r) of 9.4%, 0.9% and 0.4%, respectively, with respect to the real values, verifying the validity of the simulations carried out. From a trade-off between performance (reflection and losses) and robustness of the sensor against breakage, the manufactured LIF will present an air micro-cavity with a diameter ~ 70 μm.

Based on the detailed results, the initial point of the FBG must be placed at the optimum point to limit the total length of the

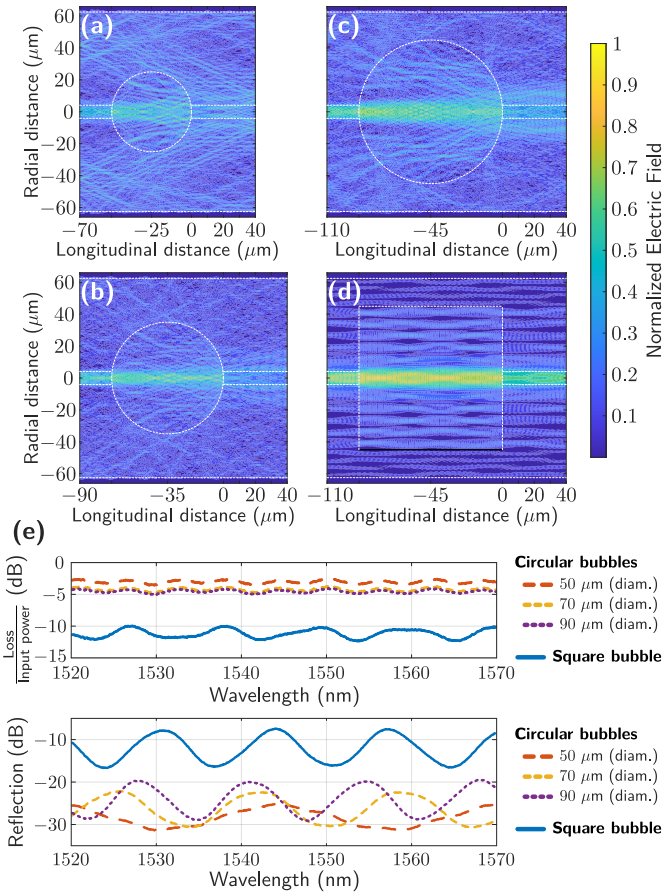

Fig. 2. Simulation of the electric field in circular air cavities of diameter 50 μm (a), 70 μm (b) and 90 μm (c) within an SMF, together with the ideal case of a square bubble with 90 μm side (d). Loss and reflection spectrum for each case is presented (e).

LIF sensor, while maximizing its reflection performance. Consequently, the following function $E^\star(x)$ is defined, which refers to the average electric field (in wavelength) in the longitudinal axis of the fiber ($y = z = 0$) (COMSOL cutline core is required):

$$E^\star(x) = \frac{1}{50\ \mathrm{nm}} \int_{1520\ \mathrm{nm}}^{1570\ \mathrm{nm}} |E(\lambda, x, y = 0, z = 0)| \mathrm{d}\lambda, \qquad \textbf{(2)}$$
$$\forall\, x, \lambda \in \mathbb{R} : 1520\ \mathrm{nm} \leq \lambda \leq 1570\ \mathrm{nm}.$$

where $E(\lambda, x, y, z)$ refers to the electric field. The reference point on the X axis ($x = 0$) is located at the end of the air micro-cavity.

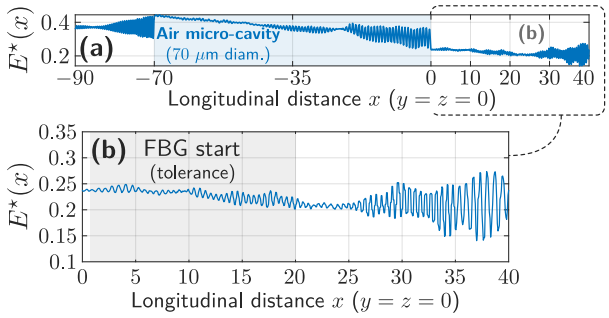

Fig. 3. Simulated $E^\star(x)$ value (Eq. 2) in circular air cavity of 70 μm diameter (a), with the section after the bubble emphasized ($0 - 40$ μm) (b).

In Fig. 3, it is depicted the value of $E^{\star}(x)$ for the simulated ⌀70 μm circular air cavity (bubble later manufactured). Focusing on the section after the bubble (Fig. 3(b)), the electric field is seen to be more confined to the core center ($y = z = 0$) in the first $\sim$ 20 μm (the final interference is due to the simulation fiber end, located at 40 μm). This aspect is also slightly appreciated in Fig. 2(b). In order to maximize reflection efficiency, it is important to take advantage of this area by locating the beginning of the FBG.

A commercial fs fiber laser from CALMAR has been used for the inscriptions made in the experimental work detailed in this Letter. The operating wavelength is 1030 nm, with a pulse duration of 370 fs, and a maximum pulse energy (E_p) of 5 μJ. The beam is tightly focused with a long working distance objective lens from Mitutoyo (NA = 0.42). The fiber samples are mounted on a high-precision air-bearing XYZ translation stage (Aerotech) that allows controlled movement during the inscription procedure. In order to avoid the cylindrical aberrations inherent to the fiber, it is surrounded by an index-matching oil [9].

The manufacturing process of the sensor device can be divided into three differentiated stages: in-fiber air microcavity generation, fiber end tapering, and inscription of the Pl-b-Pl FBG. The stages are depicted schematically in Fig. 4.

Since the subsequent FBG inscription will be done with the fs laser, it is also used to generate the bubble inside the fiber. In this way, the use of special optical fibers (hollow core fibers, photonic crystal fibers) is avoided, as well as the dangerous acid corrosion in case of using chemical etching. Initially, there are two cleaved Corning SMF-28 sections. In the core of one end-face section a micro-hole is made with the fs laser. Both the hole properties and the splice characteristics (time and current of the electric arc discharge) determine the air-cavity size [7]. In order to obtain the optimum diameter given by the numerical model, the necessary laser inscription parameters are determined empirically. A 3 μm diameter micro-hole is generated from 120 pulses with E_p = 2.7 μJ (Fig. 4(a)). Then, based on a commercial fusion splicer (Fujikura FSM-100P), a splice is performed using an arc of 1500 ms and 25% of the maximum current (Fig. 4(b)). The result of the splice is a 72 μm diameter in-fiber air cavity (Fig. 4(c)). After manufacturing a set of 10 bubble samples, the repeatability is characterized by a standard deviation of 3.76 μm.

The second stage in the manufacturing process refers to the non-adiabatic tapering of the fiber end. The splice electrodes are placed 300 μm apart from the location of the in-fiber bubble.

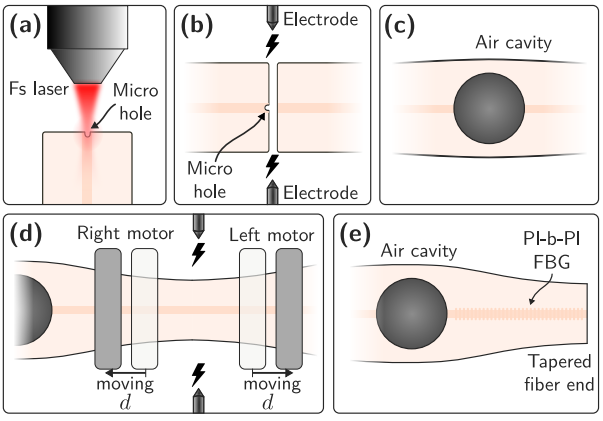

Fig. 4. Schematic of the LIF sensor manufacturing process: in-fiber air microcavity generation (a, b, c), fiber end tapering (d), and Pl-b-Pl FBG inscription (e).

Subsequently, an electric arc discharge of 3000 ms and 15% of the maximum current is applied. While performing the arc, the right and left fiber holders move backward to each other a distance d in order to apply an axial tensile stress (Fig. 4(d)). Parameter d defines the subsequent waist of the tapered fiber generated. In this Letter, after a series of tests performed, d = 30 μm is applied, causing a diameter of the fiber end of $\sim$ 75 μm.

Finally, the fiber is cleaved and an FBG is inscribed between the point determined by simulation and the fiber end. The plane-by-plane inscription method is used, which is achieved by means of the slit beam shaping technique [10]. With this, a 200 μm FBG is inscribed 18 μm after the bubble. The period is Λ = 1.61 μm, which generates the 3rd order in the C-Band (around 1545 nm). The pulse energy of the laser is 5 μJ. However, only 25.1% crosses the slit and is absorbed non-linearly by the fiber. This is because the slit width is 400 μm, while the diameter of the Gaussian laser beam is 2.5 mm ($1/e^2$). According to the measurements made with the quantitative phase microscopy (QPM) technique, the Type I RIC estimated for the modifications generated with the fs laser is $\Delta n \simeq 5 \cdot 10^{-3}$ ($\Delta n \propto \Delta\phi$, with ϕ being the induced phase change) [10]. A slightly greater Δn is undertaken to maximize the grating reflection, at the cost of slightly increasing the losses.

Once the optical fiber sensor is manufactured, it is inserted into a ⌀400 μm surgical needle, and is fixed using epoxy resin. It is important to note that the sensor, being located near the fiber end, is susceptible to breakage when contacting solid surfaces. Consequently, the fiber end-face is placed $\sim$ 200 μm before the needle end. In this way, the needle itself acts as a fiber protection. Another option would be to place the FBG before the bubble, so that changes of the end-face do not vary the sensor response.

During the inscription, the reflection spectra of the different manufacturing stages are obtained using a broadband light source (HP 83437A) and an optical spectrum analyzer (Anritsu MS9740A, 30 pm resolution). The spectra measured after finishing the manufacturing stages (c) and (e) are depicted in Fig. 5(b). Likewise, the simulation result of the complete lab-in-fiber sensor (after (e) stage) is shown, verifying the experimental result. Detection of the FBG peak position is performed by first decoupling the contribution of the interference pattern, and then applying a threshold-based center of gravity (COG) algorithm [11].

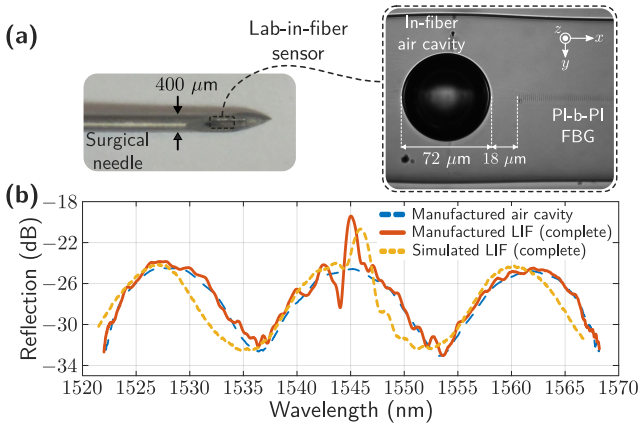

Fig. 5. Microscope images of LIF sensing elements: in-fiber air micro-cavity and Pl-b-Pl FBG, and its integration into the ⌀400 μm surgical needle (a). Reflection spectra of the complete LIF sensor, both manufactured and simulated, as well as that corresponding only to the manufactured air cavity (b).

The measurement procedure is detailed below. The lab-in-fiber sensor essentially consists of two sensor elements: the in-fiber air microcavity and the Pl-b-Pl FBG. The air bubble is only sensitive to axial strain (insensitive to SRI and temperature, and protected from radial strain by the needle), and has an FSR that takes a value of 16.58 nm (Fig. 5(b)). This FSR value offers a cavity length of 71.98 μm according to Equation 1 ($\epsilon_r = 0.03\%$), which is consistent with the measurement obtained from the picture of Fig. 5(a). On the other hand, FBG is sensitive to both axial strain and SRI (due to fiber end tapering). As it is also sensitive to temperature, in its application the temperature must remain stable compared to that taken as a reference.

However, it should be noted that a second cavity between the bubble and fiber end is also strictly manifested in the spectrum. It has a cavity length of ~ 218 μm (FSR = 3.75 nm), being slightly sensitive to axial strain and SRI. Despite this, such a low FSR value induces high measurement errors, and it is additionally dispensable for this two-parameter detection, so it will not be taken into account. Therefore, the detection problem can be expressed mathematically as follows:

$$\begin{bmatrix} \Delta\lambda_B \\ \Delta\ \mathrm{FSR} \end{bmatrix} = \begin{bmatrix} (\kappa_\varepsilon)_{\mathrm{FBG}} & (\kappa_{\mathrm{SRI}})_{\mathrm{FBG}} \\ (\kappa_\varepsilon)_{\mathrm{FP}} & \cancelto{0}{(\kappa_{\mathrm{SRI}})_{\mathrm{FP}}} \end{bmatrix} \begin{bmatrix} \Delta\varepsilon \\ \Delta\ \mathrm{SRI} \end{bmatrix}, \tag{3}$$

where κ_ε and κ_{SRI} are the axial strain and SRI sensitivities, respectively, both being specified for the FBG and the in-fiber bubble (Fabry-Perot cavity, FP). $\Delta\lambda_B$ refers to the Bragg wavelength shift, and ΔFSR corresponds to the FSR variation of air cavity.

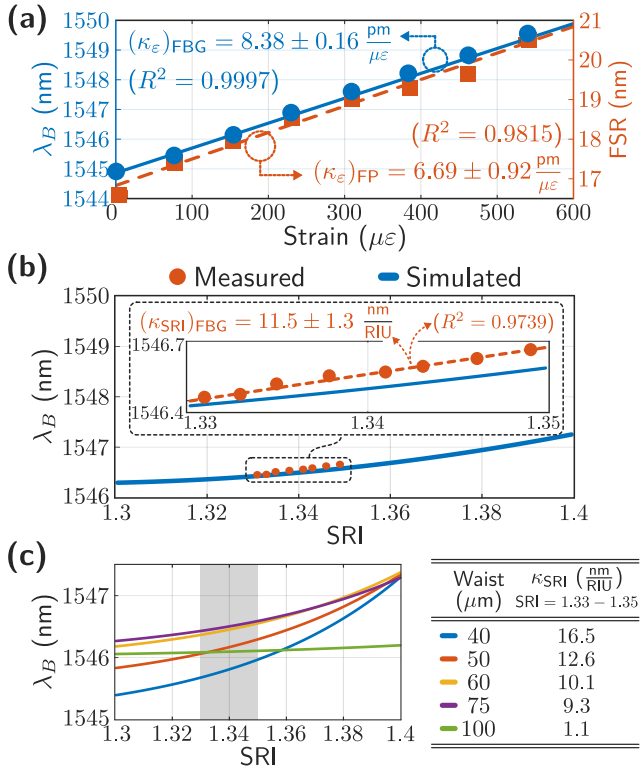

Fig. 6. Measured axial strain sensitivity of air cavity ($(\kappa_\varepsilon)_{\mathrm{FP}} = 6.69$ pm/$\mu\varepsilon$) and FBG ($(\kappa_\varepsilon)_{\mathrm{FBG}} = 8.38$ pm/$\mu\varepsilon$) (a). Simulated (1.3 − 1.4) and measured (1.33 − 1.35) SRI sensitivity ($(\kappa_{\mathrm{SRI}})_{\mathrm{FBG}} = 11.5$ nm/RIU) of the FBG (b). COMSOL simulation of the sensor's SRI sensitivity for different taper waist diameter (c).

To obtain the different sensitivities (κ_), measurement sets have been carried out both in axial strain and in the surrounding refractive index (with different concentrations of sugar in water). The results obtained are depicted in Fig. 6. The strain measurement setup is as follows: the fiber end is fixed, and a fiber point located 13 cm from the end is fixed to a translation stage. A tensile strain is applied to the LIF sensor by moving the translation stage away from the fixed one in steps of 0.01 mm (at room temperature). The axial strain suffered by the sensor when touching an object/tissue has been determined to vary between 200 and 400 $\mu\varepsilon$. On the other hand, λ_B shift due to SRI has been experimentally measured in the range $1.33 - 1.35$, and simulated using COMSOL (Finite-Element Frequency-Domain, FEFD) in the range $1.3 - 1.4$. Likewise, the response of the sensor to the SRI for different waist diameter of the non-adiabatic tapered fiber has also been evaluated using COMSOL FEFD simulations 6(c). The trade-off that exists between robustness and SRI sensitivity is observed. A more abrupt tapered fiber end (lower waist) causes more interaction of the modal field with the area around the fiber, increasing sensitivity.

In conclusion, this Letter presents the design, simulation, and manufacture of a lab-in-fiber sensor located at the end of an SMF, and integrated into a surgical needle. The sensor is less than 300 μm in length and consists of an in-fiber air micro-cavity and a plane-by-plane FBG inscribed using an fs laser. The reflection detection mode allows its application in biomedical environments, being minimally invasive in the measurement process. The operation principle of this first prototype follows the "*touch and measure*" approach, allowing the surrounding refractive index of a fluid to be detected when the sensor contacts an object/tissue. The axial strain (*touch*) and SRI (*measure*) sensitivities are 6.69 pm/$\mu\varepsilon$ and 11.5 nm/RIU (SRI = $1.33 - 1.35$), respectively.

Funding. FEDER funds of European Comission, and Spanish Government (TEC2016-76021-C2-2-R); PhD grant by Spanish Government (FPU2018/02797).

Acknowledgments. The authors thank F. Algorri for helpful discussions in the simulation designs.

Disclosures. The authors declare no conflicts of interest.

REFERENCES

1. J. Wu, M. Dong, C. Rigatto, Y. Liu, and F. Lin, npj Digit. Medicine **1**, 1 (2018).
2. M. Rahman, M. A. Stott, Y. Li, A. R. Hawkins, and H. Schmidt, Optica **5**, 1311 (2018).
3. M. Haque, K. K. C. Lee, S. Ho, L. A. Fernandes, and P. R. Herman, Lab Chip **14**, 3817 (2014).
4. A. Madani, S. M. Harazim, V. A. B. Quiñones, M. Kleinert, A. Finn, E. S. G. Naz, L. Ma, and O. G. Schmidt, Opt. Lett. **42**, 486 (2017).
5. M. Malinauskas, A. Žukauskas, S. Hasegawa, Y. Hayasaki, V. Mizeikis, R. Buividas, and S. Juodkazis, Light. Sci. & Appl. **5**, e16133 (2016).
6. C. R. Liao, Y. Wang, D. N. Wang, and M. W. Yang, IEEE Photonics Technol. Lett. **22**, 1686 (2010).
7. C. Liao, L. Xu, C. Wang, D. N. Wang, Y. Wang, Q. Wang, K. Yang, Z. Li, X. Zhong, J. Zhou, and Y. Liu, Opt. Lett. **38**, 4473 (2013).
8. S. Liu, K. Yang, Y. Wang, J. Qu, C. Liao, J. He, Z. Li, G. Yin, B. Sun, J. Zhou, G. Wang, J. Tang, and J. Zhao, Sci. Reports **5**, 7624 (2015).
9. Y. Lai, K. Zhou, L. Zhang, and I. Bennion, Opt. Lett. **31**, 2559 (2006).
10. P. Roldan-Varona, D. Pallares-Aldeiturriaga, L. Rodriguez-Cobo, and J. M. Lopez-Higuera, J. Light. Technol. pp. 1–1 (2020).
11. D. Ganziy, O. Jespersen, G. Woyessa, B. Rose, and O. Bang, Appl. Opt. **54**, 5657 (2015).

FULL REFERENCES

1. J. Wu, M. Dong, C. Rigatto, Y. Liu, and F. Lin, "Lab-on-chip technology for chronic disease diagnosis," npj Digit. Medicine 1, 1–11 (2018).
2. M. Rahman, M. A. Stott, Y. Li, A. R. Hawkins, and H. Schmidt, "Single-particle analysis with 2d electro-optical trapping on an integrated optofluidic device," Optica 5, 1311–1314 (2018).
3. M. Haque, K. K. C. Lee, S. Ho, L. A. Fernandes, and P. R. Herman, "Chemical-assisted femtosecond laser writing of lab-in-fibers," Lab Chip 14, 3817–3829 (2014).
4. A. Madani, S. M. Harazim, V. A. B. Quiñones, M. Kleinert, A. Finn, E. S. G. Naz, L. Ma, and O. G. Schmidt, "Optical microtube cavities monolithically integrated on photonic chips for optofluidic sensing," Opt. Lett. 42, 486–489 (2017).
5. M. Malinauskas, A. Zukauskas, S. Hasegawa, Y. Hayasaki, V. Mizeikis, R. Buividas, and S. Juodkazis, "Ultrafast laser processing of materials: from science to industry," Light. Sci. & Appl. 5, e16133–e16133 (2016).
6. C. R. Liao, Y. Wang, D. N. Wang, and M. W. Yang, "Fiber In-Line Mach-Zehnder Interferometer Embedded in FBG for Simultaneous Refractive Index and Temperature Measurement," IEEE Photonics Technol. Lett. 22, 1686-1688 (2010).
7. C. Liao, L. Xu, C. Wang, D. N. Wang, Y. Wang, Q. Wang, K. Yang, Z. Li, X. Zhong, J. Zhou, and Y. Liu, "Tunable phase-shifted fiber Bragg grating based on femtosecond laser fabricated in-grating bubble," Opt. Lett. 38, 4473-4476 (2013).
8. S. Liu, K. Yang, Y. Wang, J. Qu, C. Liao, J. He, Z. Li, G. Yin, B. Sun, J. Zhou, G. Wang, J. Tang, and J. Zhao, "High-sensitivity strain sensor based on in-fiber rectangular air bubble," Sci. Reports 5, 7624 (2015).
9. Y. Lai, K. Zhou, L. Zhang, and I. Bennion, "Microchannels in conventional single-mode fibers," Opt. Lett. 31, 2559–2561 (2006).
10. P. Roldan-Varona, D. Pallares-Aldeiturriaga, L. Rodriguez-Cobo, and J.M. Lopez-Higuera, "Slit beam shaping technique for femtosecond laser inscription of enhanced plane-by-plane FBGs," J. Light. Technol. 1-1 (2020).
11. D. Ganziy, O. Jespersen, G. Woyessa, B. Rose, and O. Bang, "Dynamic gate algorithm for multimode fiber Bragg grating sensor systems," Appl. Opt. 54, 5657-5661 (2015).